Collisional Disruption of Ice by High-Velocity Impact

Masahiko Arakawa

Institute of Low Temperature Science, Hokkaido University, Kita-ku Kita 19 Nishi 8, Sapporo 060-0819, Japan
E-mail: arak@lowtem.hokudai.ac.jp

High-velocity impact among icy planetesimals is a physical phenomenon important to the planetary evolution process in the outer Solar System. In order to study this phenomenon, impact experiments on water ice were made by using a two-stage light gas gun installed in a cold room ($-10°$C) to clarify the elementary processes of collisional disruption and to study the reaccumulation and the escape conditions of the impact fragments. Cubic ice targets ranging in size from 15 to 100 mm were impacted by a nylon projectile of 7 mg with an impact velocity (v_i) from 2.3 to 4.7 km/s. The corresponding mass ratio of the projectile to the target (m_p/M_t) ranged from 10^{-3} to 10^{-6}, which is two orders of magnitude lower than that used in previous studies (Arakawa *et al.* 1995, *Icarus* 118, 341–354). As a result, we obtained data on elementary processes such as attenuation of the shock wave and fragmentation dynamics. We found that the shock pressure attenuates in the ice target according to the relation of $P \propto (L_p/r)^2$, irrespective of the mass ratio between 10^{-3} and 10^{-5}, where L_p is the projectile size and r is a propagation distance. The largest fragment mass (m_l) normalized by the original target mass has a good relationship to a nondimensional impact stress (P_I, NDIS) defined as the ratio of the antipodal pressure to the material strength. This relationship is described as $m_l/M_t \propto P_I^{-1.7}$ for a wide range of impact conditions (50 m/s $< v_i <$ 4 km/s and $10^{-1} < m_l/M_t < 10^{-6}$), and shows the utility of NDIS. Using a measured shock wave decay constant of 2, the reaccumulation and the escape conditions of icy bodies in high-velocity collisions were estimated. As a result, it was clarified that a rubble pile could be formed when large icy bodies (radius > 20 km) reaccumulated. On the other hand, when smaller icy bodies (radius < 2 km) disrupted catastrophically, all fragments escaped and a rubble pile was never formed.   ⓒ **1999 Academic Press**

Key Words: **icy satellite; impact process; shock-wave attenuation; catastrophic disruption; reaccumulation.**

1. INTRODUCTION

Water ice, one of the most abundant molecules in the outer Solar System, is considered a main constituent material of ring particles and icy bodies such as icy satellites, comets, and Kuiper belt objects. Collision among icy planetesimals is the most important physical process in that region; the fragmentation and accretion of icy planetesimals caused by high-velocity collision resulted in a variety of the icy bodies currently observed in the outer Solar System, such as ring particles, small or large icy satellites, and cores of the giant planets. When icy bodies with a high velocity collide with each other, they are completely disrupted into small fragments under certain conditions. The fragments with ejection velocities lower than the escape velocity of the parent body can gravitationally reaccumulate to form a rubble pile. On the other hand, these high-velocity fragments can escape from the gravity field of the parent body and become the source of smaller icy satellites. Interstellar dust particles collide with Kuiper belt objects at a very high velocity beyond 10 km/s, so that the high-velocity dusts are excavated from the crater by each collision. Since the ejecta velocity is high enough for the fragments to escape the object, very little ejecta reaccumulates to become interplanetary dust particles (Yamamoto and Mukai 1998).

Numerous experimental studies on ice impacts have been conducted to investigate the physics of impact fragmentation and to construct a scaling law of the impact disruption (Kawakami *et al.* 1983; Lange and Ahrens 1987; Frish 1991; Kato *et al.* 1992, 1995; Arakawa *et al.* 1995; Arakawa and Higa 1996). Previous experimental studies on ice impacts clarified several properties of ice disruption such as mass distribution of fragments, largest fragment mass, and antipodal velocity. These results were used to develop suitable scaling laws for the impact disruption of water ice. The scaling parameters proposed by Fujiwara and Tsukamoto (1980), Housen and Holsapple (1990), and Mizutani *et al.* (1990) were tested in Arakawa *et al.* (1995) with water ice in order to check their applicability. Energy density, defined as the ratio of a projectile kinetic energy divided by the target mass, is the most popular scaling parameter to represent the degree of impact disruption. However, the physics of the relationship between the fragmentation process and this parameter is not yet clear. Mizutani *et al.* (1990) considered the elementary processes of impact disruption and proposed a scaling parameter termed nondimensional impact stress (NDIS, P_I). They included a propagation process of impact stress through the target, and compared impact stress with material strength to determine the degree of impact disruption. Thus, the meaning of this parameter is relatively clear in terms of the physics of impact fragmentation, and attenuation of shock pressure has an important role in this scaling law; however, the process of attenuation is very complicated. Arakawa *et al.* (1995) studied

shock pressure in ice, and improved the NDIS by measuring the decay constant. They noted that the decay constant varied with the impact conditions, and that a decay constant of 3 (used by Mizutani) was valid only under limited conditions for ice. Arakawa *et al.* (1995) estimated the reaccumulation condition of icy bodies after impact disruption by using the measured decay constant, although the results obtained were limited in the range of impact velocity from 50 to 600 m/s, and in the mass ratio from 0.1 to 10^{-3}. Therefore, we considered the attenuation of shock pressure under a wide range of impact conditions.

We prepared a two-stage light gas gun in a cold room to conduct impact experiments with water ice at a higher impact velocity (4 km/s) and a lower mass ratio ($\sim 10^{-6}$), and studied the attenuation of the shock pressure remotely, at a distance from the impact point, by means of ultrahigh-speed photography. We observed the collisional disruption within 1 ms to measure the antipodal velocity of targets of various sizes. The antipodal velocity was used to estimate the decay constant of ice and to derive the reaccumulation and the escape conditions of impact fragments ejected from icy bodies.

2. EXPERIMENTS

2.1. Collisional Disruption by Two-Stage Light Gas Gun

Impact experiments were conducted by using a two-stage light gas gun installed horizontally in a large cold room regulated at $-10°C$. The inner diameter of the gun barrel was 1.6 mm. This gun can accelerate a nylon projectile up to 5 km/s. The projec-

tiles were nylon cylinders, with a diameter of 1.6 mm, a height of 2.0 mm, and a mass of 7 mg. The impact velocity was from 2.3 to 4.7 km/s and the corresponding shock pressure at the impact point was from 6.5 to 14 GPa as estimated by using the impedance matching method where the Hugoniots of ice and nylon were given by Gaffney (1985) and Marsh (1980), respectively (Table I) For the targets, we used polycrystalline water ice, which was commercially delivered from Kanekin Co., Sapporo and composed of columnar crystals with a length of about 10 cm and a diameter of about 1 cm, elongated along the crystallographic *a* axis. The targets were cubes with sides of 15 to 100 mm and masses of 3.5 to 962 g. The corresponding mass ratio of the projectile to the target was from 2×10^{-3} to 7.3×10^{-6}. The projectile was impacted on the center of target surface irrespective of crystallographic axes in ice. The target was suspended by strings in the recovery box (Fig. 1) to prevent loss of the fragments and to enable direct observation of the impact disruption. The recovery box is made of stainless steel with windows of acrylic acid resin. The sides and bottom of the box were lined with urethane foam 2 cm thick in order to recover the fragments without damage. The recovery box was set in a vacuum chamber and evacuated to 900 Pa before impacts. The projectile velocity was measured by a pair of laser beams set at an interval of 5 cm. When the projectile cut these beams, a pair of photodiode detectors monitoring the laser intensity measured the signals.

After the impact experiments, we recovered all fragments in the recovery box and weighed them by using an electric mass balance under the condition of $-20°C$ (temperature low enough to avoid significant evaporation of ice fragments). All fragments

TABLE I
Experimental Conditions and Results

Run no.	V_i (km/s)	P_0 (GPa)	L_t (mm)	M_t (g)	Q (J/kg)	V_a (m/s)	V_e (km/s)	m_1 (g)	P_I	n
212-1	2.31	6.52	20	7.82	2047	31.1(0.9)	—	0.13	2.61	0.67
109-2	2.42	6.73	15	3.50	5856	26.0(2.9)	—	0.026*	2.18	0.81
114-2	3.56	9.64	15	3.52	14401	78.5(1.5)	—	0.0016*	6.58	0.70
212-2	3.48	9.4	20	7.76	5462	34.9(1.0)	—	0.041*	2.93	0.72
213-1	3.51	9.48	20	7.72	4787	44.7(3.3)	—	0.081*	3.75	0.68
108-2	3.73	10.16	20	6.50	7491	70.9(3.8)	—	0.039*	5.95	0.65
216-1	4.42	12.55	20	7.81	7504	39.6(0.9)	—	0.052*	3.32	0.73
216-2	3.57	9.67	28	19.93	1918	15.4(1.1)	—	0.21	1.29	0.73
119-2	3.93	10.82	29	21.73	2132	27.4(1.4)	—	0.26	2.30	0.67
218-1	3.39	9.13	41	63.93	539	7.03(0.93)	—	3.66	0.590	0.72
120-3	4.00	11.05	39	54.07	1035	19.3(1.4)	—	1.03	1.62	0.65
220-2	3.79	10.36	49	111.58	386	4.32(0.46)	—	6.11	0.362	0.74
1226-2	4.17	11.64	50	115.00	680	—	—	6.10	—	—
1226-3	4.70	13.63	50	115.50	669	—	3.42(0.08)	4.80	—	—
218-2	4.13	11.5	60	198.09	258	—	2.75(0.03)	6.42	—	—
219-1	3.95	10.88	69	303.82	179	—	2.60(0.04)	27.35	—	—
218-3	3.90	10.72	82	510.78	104	—	3.03(0.05)	66.27	—	—
220-1	3.89	10.68	91	690.61	65.7	—	3.15(0.04)	237.84	—	—
219-2	3.97	10.95	101	962.03	57.3	—	3.50(0.08)	906.9	—	—

Note. n is defined as $b/3$, where b is the decay constant of the shock pressure. m_1 with a symbol of * is estimated from the fragment size. V_e is the maximum velocity of the ejecta fragments excavated from the crater. The values in parentheses in the columns of V_a and V_e show the standard errors in determination of these velocities.
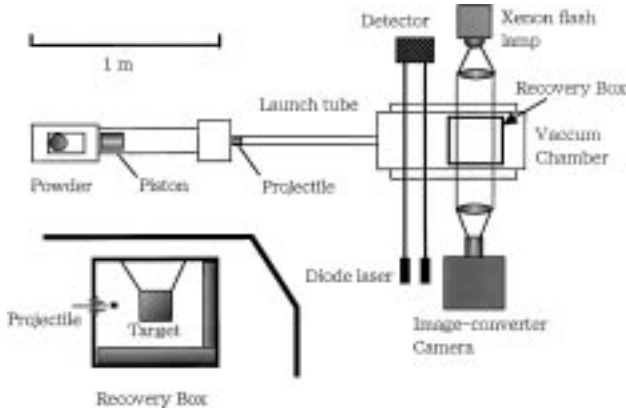
FIG. 1. Schematic illustration of the experimental apparatus. The enlarged figure of the recovery box is shown on the left.

were weighed in order to derive a mass distribution for those targets larger than 5 cm. Fragments smaller than 0.1 g were sifted into seven categories, and the number of these fragments and the average mass were estimated for each category. For targets smaller than 4 cm, only the largest fragments were weighed. When the largest fragments were near to or lighter than the limit of the electric balance (0.01 g), their weight was estimated by their size. We measured the fragment size for three different directions and calculated the mass by assuming a rectangular parallelepiped with three measured edges. This estimate may tend toward the upper limit of the fragment mass because of the fragment's shape, which is likely to be ellipsoidal.

2.2. Ultrahigh-Speed Photography

The collisional disruption was observed by means of ultrahigh-speed photography. We used an image converter camera (Ultra NAC, Japan) which can take 24 successive images up to the time interval of 500 ns. We changed the time interval between images from 2 to 100 μs, so that a wide range of fragment velocity, from 5 km/s to 5 m/s, could be measured. The exposure time was 100 ns; a completely still image could be obtained even though the fragment velocities are faster than 1 km/s. In order to use this short exposure time, a xenon flash lamp with the power of 50 J per flash (J/F) was used for the lighting. This flash lamp has a long duration of about 1 ms, which was necessary to measure a fragment velocity slower than 100 m/s. The shadow photograph lighting system, which employs a pair of lenses (see Fig. 1), is very suitable for the study of fine, high-velocity fragments, since the lighting system is highly sensitive to spatial density variations. Therefore, our measurement system can completely cover the velocity range of fragments created by impact disruption; it allows observation not only of cratering ejecta with velocities faster than 1 km/s but of the largest fragment with velocity slower than 100 m/s. Given that the ejection velocity of fragments is faster than 5 m/s for samples smaller than 5 cm, we can observe the entire fragment velocity for these samples. In the case of samples larger than 6 cm, only the ejecta near the impact point were observed in order to study the cratering process.

The most important feature of the image converter camera was a trigger. For 24 successive images with an interval of 5 μs, the total recording time is 120 μs. The reproducibility of a trigger system (i.e., within a few tens of microseconds) is necessary to obtain a good image. Thus, we used the velocity measurement system for the trigger, because the projectile signal observed had a very narrow pulse (shorter than 3 μs) and was therefore suitable as a the trigger signal. The camera observed the sample perpendicular to the impact direction, so that the sample appeared square. Because the surface of the sample was rough, incident parallel light collimated by the lens was scattered by the surface; the sample looked like a black shadow in this lighting system. The position of the sample was regulated by changing the length of the strings and was set such that the projectile impacted at the center of the sample surface facing the gun barrel.

When the impact fragments were too small to be recognized in the image, we only observed an expansion of the envelope formed by the fragments. In this study, we measured the velocity of these envelopes as expanding from each initial position. Specifically, we used the antipodal point to measure the expansion velocity of the envelope. The antipodal velocity is used in reference to the degree of impact disruption and has been measured for basalt and for water ice in previous studies. Ejecta velocity during the cratering process was also measured.

3. SCALING PARAMETER

Energy density (Q) is a popular scaling parameter to describe the degree of collisional disruption. This parameter is defined as the ratio of the projectile kinetic energy to the target mass, $Q \equiv \frac{1}{2}\frac{v_i^2 m_p}{M_t}$. However, a more convenient parameter based on shock physics was proposed by Mizutani *et al.* (1990), called the nondimensional impact stress. This parameter is defined as

$$P_I = P(L_t)/Y, \qquad (1)$$

where $P(L_t)$ is the shock pressure at the antipodal boundary of the target, L_t is the target size, and Y is the target strength. Lange and Ahrens (1983) measured the dynamic tensile strength of water ice at a strain rate of about 10^4 s^{-1}, and reported that it was about 17 MPa. We use this value for Y. $P(L_t)$ is usually described by using several empirical parameters: the decay constant of the shock pressure (b), the size of the isobaric core, and the depth of the center of the isobaric core. Mizutani *et al.* (1990) simplified the description of $P(L_t)$ as

$$P(L_t) = P_0(L_p/L_t)^b. \qquad (2)$$

The decay constant 3 is used in the theory of Mizutani *et al.* (1990). Arakawa *et al.* (1995), however, clarified that the decay constant for water ice varied between 2 and 3 in relation to the impact velocity and mass ratio. Arakawa *et al.* (1995) improved the nondimensional impact stress parameter using the measured decay constant for ice rather than using a constant value of 3.

To analyze the data and by using the respective masses of the projectile and the target, Eq. (2) can be rewritten as

$$P(L_t) = P_0 \left(\frac{m_p \, \rho_t}{M_t \, \rho_p} \right)^{b/3}, \qquad (3)$$

where ρ_t and ρ_p are the densities of the target and the projectile, respectively.

$P(L_t)$ can be derived from the measured antipodal velocity. When the particle velocity in the target (u_p) is low enough, relative to the bulk sound velocity (C_t) of water ice (3110 m/s, Gold 1958), the shock pressure is calculated by the equation $P = \rho_t C_t u_p$. u_p at the antipodal point can be estimated from the antipodal velocity (V_a) by using the free-surface approximation $u_p = \frac{1}{2} V_a$. Then we can obtain the antipodal shock pressure for targets of different size according to the equation

$$P(L_t) = \rho_t C_t V_a / 2. \qquad (4)$$

The decay constant b can be calculated from the combination of Eqs. (3) and (4) when P_0 is determined from the impact velocity by using the impedance matching method with Hugoniots of the nylon projectile and water ice. The decay constant derived from this procedure is the average through the entire target. However, in the results of several numerical simulations (Ahrens and O'Keefe 1977, Pierazzo *et al.* 1997), the decay constant was found to change relative to distance from the impact point. Therefore, we used another analytical procedure to determine the decay constant dependent on distance. In this procedure, we assumed that the target size and the antipodal pressure were equivalent to the propagation distance of the shock wave and the shock pressure at that distance, respectively. As a result, we can study the attenuation of shock pressure by examining the relation between the target size and the antipodal pressure. These two procedures were used to investigate shock wave propagation.

4. RESULTS AND DISCUSSIONS

4.1. Collisional Disruption Process

Figure 2 shows a photograph taken by the image converter camera for an ice target with a size of 20 mm impacted at 3.5 km/s (Run 212-2). The square black area is the cubic target, suspended by strings. The projectile just before impact can be seen on the image at 4 μs, and collision occurs at the center of the target surface at 8 μs. The high-velocity fine fragments were ejected from the impact point in opposite direction to the impact with a velocity greater than 1 km/s. The ejecta flow from the crater creates an ejecta curtain at an angle of 60° to the impact surface. This excavation flow makes a large crater on the impact surface and blows away the surface to the left side with a velocity dependent on the distance from the impact point. At 70 μs after impact, the target begins to expand like a balloon, and inside this ballooning "envelope" the fragments expand radially from

the impact center with a velocity dependent on distance from the center. Minimum ejection velocity in the observed envelope usually occurs at the antipodal point. The rear surface moves with almost the same velocity at all positions, but the formation of irregular surface can be observed after 70 μs. In this case, a minimum ejection velocity of 35 m/s is observed near the antipodal point. We measured the antipodal velocity applying this kind of photography to a target 15 to 50 mm in size; then when the irregular surface appeared, we measured the minimum velocity at the rear surface rather than the velocity at the antipodal point. The standard error to determine the antipodal velocity is also shown in Table I, and this error is almost attributable to the image analysis.

We observed the crater formation process for targets larger than 60 mm and measured the growth velocity and the shape of the ejecta curtain. Figure 3 shows the observed image of crater formation for Run 220-1. We could see the curved trajectories in the crater ejecta in the first frames, from 4 to 12 μs. These trajectories, however, could not always be observed. This finding clarified that the shape of the ejecta curtain strongly depends on how the projectile impacts. In some cases, the projectile tilted as it hit the surface; Fig. 2 shows a projectile rotation of 90° before impact. The angle of the ejecta curtain to the impact surface varied from 14° to 68°. The detailed mechanism by which the curtain is shaped seems complicated and cannot at this point be explained. However, we did find that the maximum growth velocity of the ejecta curtain was an almost constant 0.7–0.9 of the impact velocity, which indicates that ejection velocity is always slower than the impact velocity (Table I). Therefore, the observed ejecta curtain may not be attributable to jetting from the boundary between the nylon projectile and the ice target, but to excavation flow from the crater (McKinnon 1989).

4.2. Antipodal Velocity and Pressure Attenuation

Figure 4 shows the results of the measurements of antipodal velocity; the velocity is plotted against the energy density. Previous results on ice and on basalt are also plotted on the figure. Our data are fitted by a least-square method and the results are shown in the figure. The relation is described by

$$V_a = 10^{-1.0 \pm 0.3} Q^{-0.71 \pm 0.09}. \qquad (5)$$

The slope of the fitted line is consistent with the relation derived by Fujiwara and Tsukamoto (1980) for basalt within the error, but our data yielded an intercept 2–3 times larger than that of the basalt. The impact conditions between our experiments and theirs are similar in terms of projectile material, impact velocity (2–4 km/s), and mass ratio of the projectile to the target (10^{-3}–10^{-6}). Therefore, the difference between values for the antipodal velocity may be caused by differences of material properties and therefore in the resulting shock propagation. The results of ice at a low-velocity impact are also plotted for comparison. Figure 4 suggests a complicated dependence on impact conditions. For instance, ice ball targets with a mass ratio of
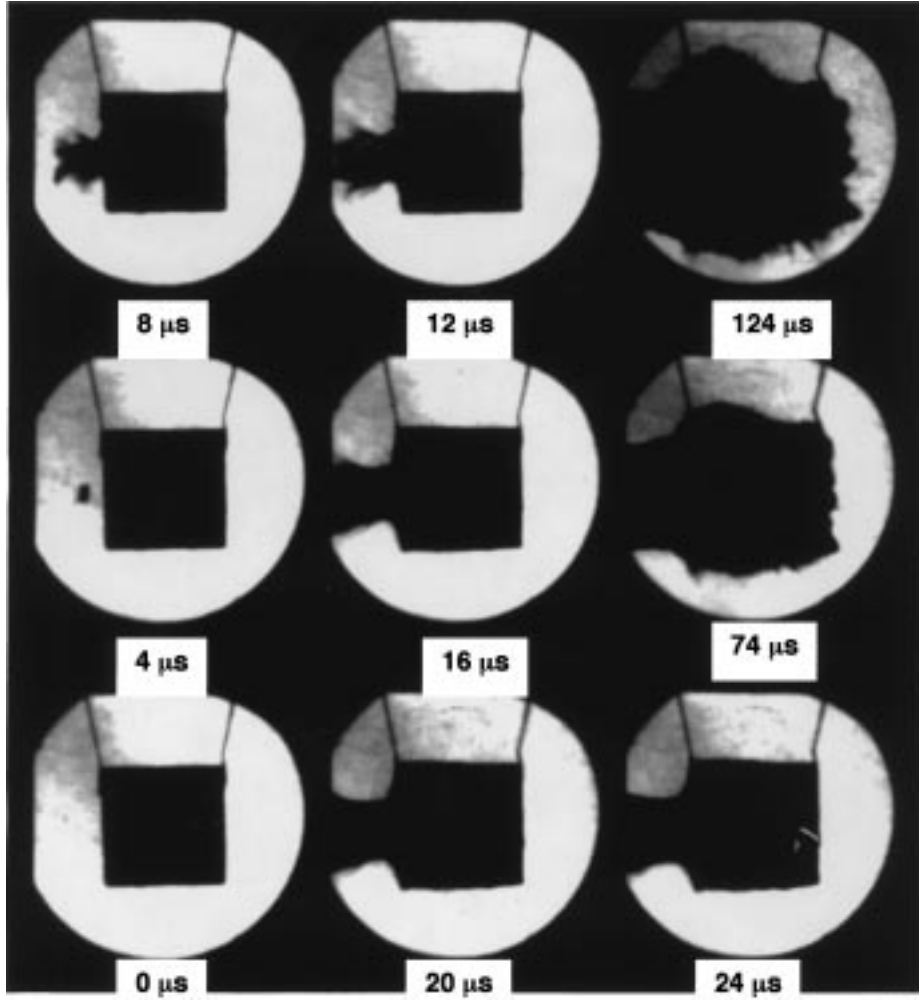
FIG. 2. Successive images of the impact disruption taken by the image converter camera for Run 212-2. The target size is 20 mm and the impact velocity is 3.48 km/s. Time is indicated below each image.

0.12 (open circle) almost overlap with the basalt and the ice cube targets with a mass ratio of 0.1 (open triangle), and clearly differ from ice cube targets with a mass ratio of 0.003 (closed triangle), although the energy density is in the same range. Our results are inconsistent with those of high mass ratio (0.12) impacts in the energy density range of 10^3–10^5 J/kg, and have higher values. These differences may be due to the complexity of attenuation of shock pressure. Arakawa *et al.* (1995) noted that the power index b of Eq. (2), which is the decay constant of the shock pressure, changed from 2 to 3 in relation to the mass ratio. We must clarify the attenuation property of the shock pressure in a wide range of impact conditions to understand these complicated relations.

Figure 5 shows the relationship between the antipodal velocity and the target size at a constant impact velocity of 3.9 ± 0.4 km/s. Antipodal velocity decreases from 100 m/s to several meters per second with increasing target size. That relation is described by

$$V_a = 10^{4.6 \pm 0.4} L_t^{-2.2 \pm 0.3}. \qquad (6)$$

This relation can be used to estimate the attenuation of the shock pressure as explained in Section 3. The antipodal shock pressure corresponding to the antipodal velocity is shown on the right side (see figure). The relation of the shock pressure vs the propagation distance of the shock pressure can be estimated as $P \propto r^{-2.2}$ according to Eq. (6). The estimated decay constant 2.2 is only valid for a propagation distance larger than 15 mm, which is approximately seven times as large as the projectile.

We can estimate the average decay constant by using the method described in Section 3. Figure 6 shows the relation between the power index (n) defined as $n \equiv b/3$ and the mass ratio of the projectile to the target, and the previous results of Arakawa *et al.* (1995) and of Arakawa and Higa (1996) are plotted in the same figure. In a previous study, the power index n was found to decrease from 1.2 at an impact velocity of 100 m/s to 0.7 at 530 m/s. Further, the power index exhibits marked dependence on the mass ratio. However, the value of n in this experiment is almost constant, and well approximates results with velocities of 410 and 530 m/s despite the large difference between values
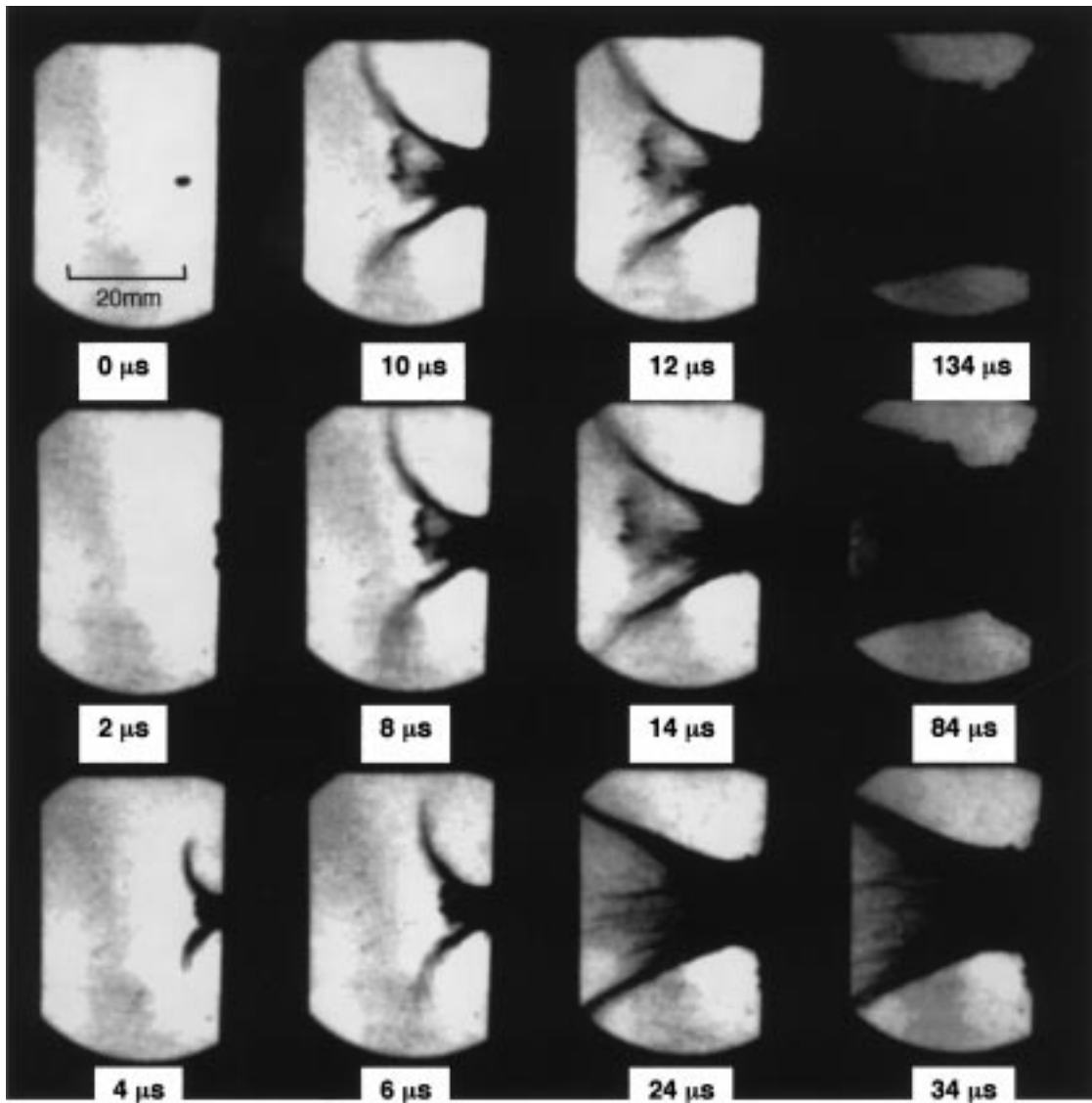
FIG. 3. Successive images of impact cratering, taken by the image converter camera for Run 220-1. The target size is 90 mm and the impact velocity is 3.89 km/s. Time is indicated below each image. A scale shown on the first image is 20 mm.

for impact velocity. The n is about 0.7 irrespective of the wide range of mass ratio (from 10^{-3} to 10^{-5}). This comparison tells us that the average decay constant is about 2 for a wide range of impact velocities from 410 m/s to 4 km/s and mass ratios from 10^{-2} to 10^{-5}.

The average decay constant is consistent with the decay constant derived from shock pressure dependent on propagation distance. This result suggests that the shock pressure attenuates at a decay constant of about 2 throughout the target. Pierazzo *et al.* (1997) evaluates the decay constant and the size of the isobaric core for ice targets by means of numerical simulation. They showed that the decay constant was about 2 and the size of the isobaric core was almost equivalent to projectile size, although the simulated impact velocity of 10 km/s was somewhat larger

than that used in our experiment and their results demonstrated a clear dependence on impact velocity.
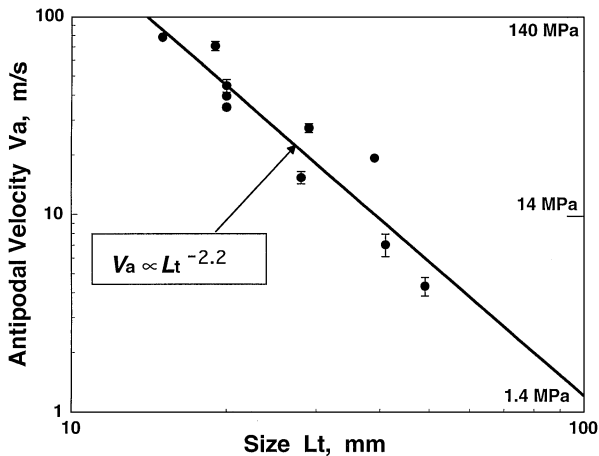
4.3. Mass Distribution of Fragments

Figure 7 shows a photograph of the recovered fragments of Run 219-1; the target suffered a catastrophic disruption. The ratio of the largest fragment mass to the original mass is 0.09, and the relation of the cumulative mass number to the fragment mass normalized by the original target mass is shown in Fig. 8. The cumulative number rapidly increases from 1 to 5, after which it increases linearly and the relation is described by a power law with a power index of 0.7. This value, 0.7, is slightly lower than that included in the results of Kato *et al.* (1995) for an ice target
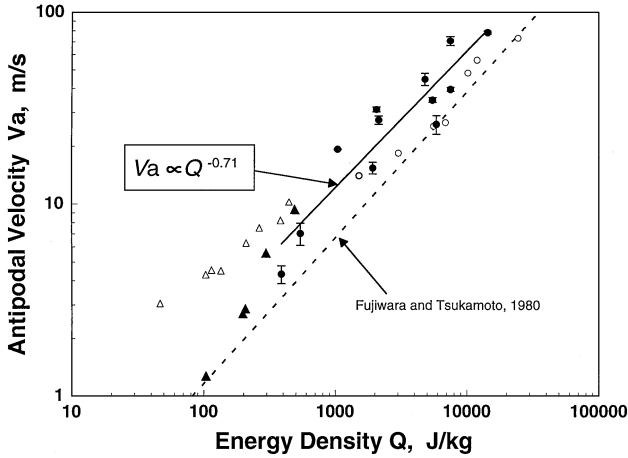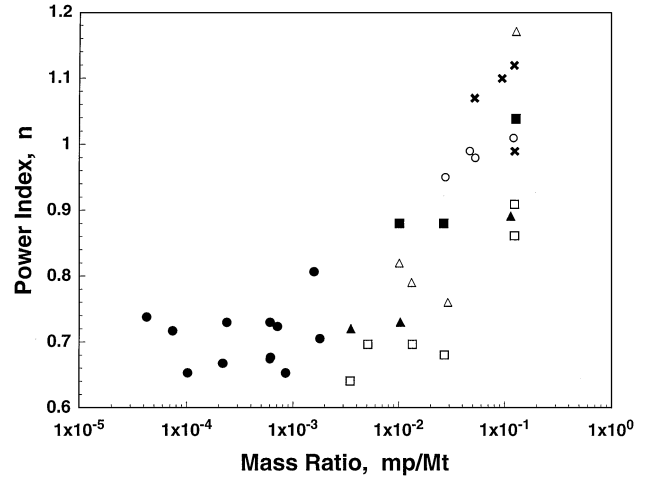
FIG. 4. The relationship between the antipodal velocity and the energy density. The data from Arakawa *et al.* (1995) (ice cube: $\triangle$, $m_p/M_t = 0.1$ (<100 m/s); $\blacktriangle$, $m_p/M_t = 0.003$ (200–600 m/s)) and Arakawa and Higa (1996) (ice ball: $\bigcirc$, $m_p/M_t = 0.12$ (100–500 m/s)) are also plotted for comparison (ice cube: $\bullet$, this study). Data were obtained at impact velocities slower than 600 m/ s for ice-on-ice impacts. Fujiwara and Tsukamoto (1980) show the results on the disruption of basalt. The error bars show the standard errors in determination of the antipodal velocity.

FIG. 6. Power index n ($n \equiv b/3$) vs mass ratio at a constant impact velocity. n is calculated from Eqs. (3) and (4). This study: $\bullet$, 2–4 km/s. Arakawa *et al.* (1995) and Arakawa and Higa (1996): $\square$, 530 m/s; $\blacktriangle$, 410 m/s; $\triangle$, 330 m/s; $\blacksquare$, 250 m/s; $\bigcirc$, 170 m/s; $\times$, 100 m/s.

0.7–0.9 by an impact velocity slower than 900 m/s. They studied the properties of mass distribution in detail and divided the distribution into three regions according to an idea proposed by Takagi *et al.* (1984). Mass distribution for targets of other sizes is also shown in Fig. 8. The slope of each distribution is calculated as 0.64($\pm$0.06) for the average in the small normalized mass region defined as region III by Kato *et al.* (1995). The total number of fragments varies among these results, and the number of fragments from the 50-mm sample is one order of magnitude larger than that of the 100-mm sample. It is well known that

the slopes representing distribution in regions I and II change in relation to impact conditions. In our study, we found that the slope increased with decreasing sample size.

Figure 9 shows the relation between the largest fragment mass normalized by the original target mass (m_1/M_t) and the energy density. The normalized largest fragment has a good power-law relation to the energy density described as

$$m_1/M_t = 10^{1.1\pm0.2} Q^{-0.91\pm0.08}, \tag{7}$$

where the correlation coefficient of this fitting is 0.94. The calculated power index 0.91 is smaller than that of 1.3 obtained by Arakawa *et al.* (1995). However, the data fluctuation for larger

FIG. 5. Target size dependence of the antipodal velocity for the impact velocity of 3.9 km/s. This relation also shows the attenuation of the shock pressure with a decay constant of 2.2. The error bars show the standard errors in determination of the antipodal velocity.

FIG. 7. Photograph of the recovered sample for Run 219-1. The target size is 70 mm and the impact velocity is 3.95 km/s. The normalized largest fragment mass is 0.090.
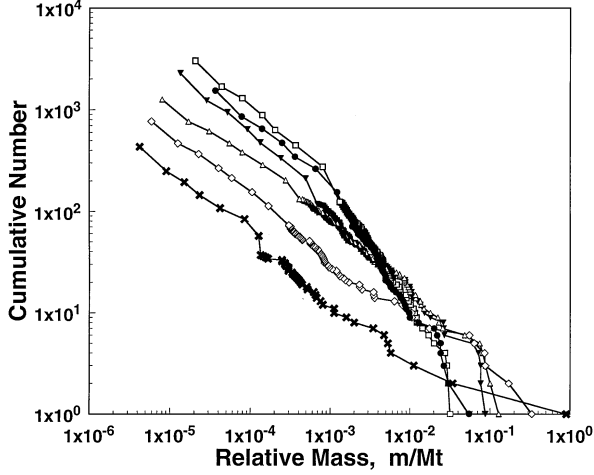
FIG. 8. Cumulative number of recovered fragments for the target with sizes from 50 to 100 mm. The impact velocity is almost constant, at 3.9 km/s. Each fragment mass is normalized by the original target mass (M_t). Run 220-2, 50 mm, ●; 218-2, 60 mm, □; 219-1, 70 mm, ▼; 218-3, 80 mm, △; 220-1, 90 mm, ◇; 219-2, 100 mm, ✕.

fragments is so large, our data falls within the fluctuation they establish; our data are consistent with the lower limit of theirs. These large fluctuations may come from the complicated dependence of the decay constant on the impact conditions, as suggested by Fig. 6. In order to see beyond this complicated behavior, we studied the relationship between the antipodal shock pressure and the normalized largest fragment; Fig. 10 shows the relation between m_1/M_t and NDIS (Table I) in conjunction with the previous data. Our data nearly approximate the extrapolated line from the previous results. All data including Arakawa *et al.* (1995) are fitted by the equation

$$m_1/M_t = 10^{-1.3 \pm 0.1} P_I^{-1.7 \pm 0.1}, \qquad (8)$$

where the correlation coefficient of this fitting is 0.87. This re-
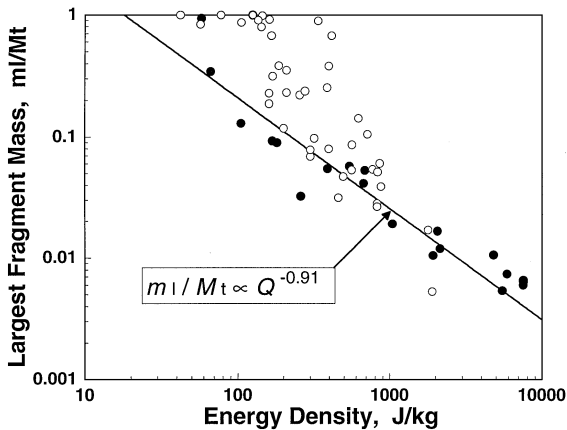

FIG. 9. Normalized largest fragment mass vs energy density. The largest fragments are clearly fitted by the power-law relation with a power index of −0.91. ○, Arakawa *et al.* (1995); ●, this study.
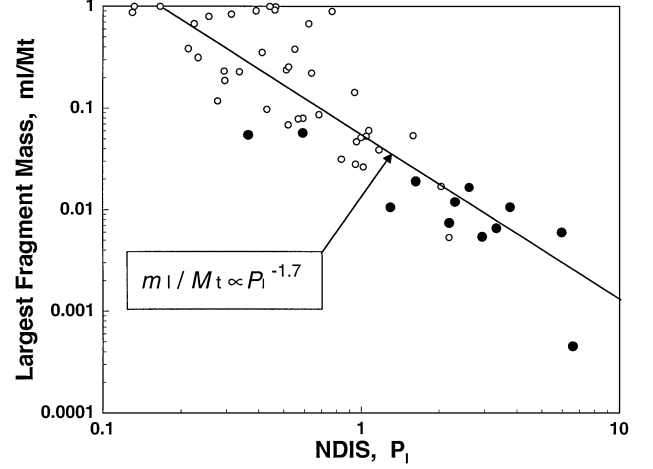

FIG. 10. Normalized largest fragment mass vs nondimensional impact stress (P_I). Our data and the previous data by Arakawa *et al.* (1995) are fitted together by the power-law relation with the power index of −1.7. ○, Arakawa *et al.* (1995); ●, this study.

lation is valid for a wide range of impact conditions, including an impact velocity from 50 m/s to 4 km/s and a mass ratio from 10^{-1} to 10^{-5}.

4.4. Fragmentation Modes

A core type disruption is commonly observed for the high-velocity impact of basalt (Fujiwara *et al.* 1977). In contrast, a cone-type disruption is usually observed for the lower velocity impact of basalt (Takagi *et al.* 1984). We cannot identify any core fragment in our experiments. As shown in Fig. 7, the large recovered fragments clearly came from the antipodal surface, not from the interior. We took a thin section of the largest recovered fragment of Run 219-2 in order to observe a crack structure formed by the shock pressure. We can infer the fragment shape from the observed cracks, and, further, check whether the observed cracks correspond to a clear core fragment at the center of the target. There are several vertical and horizontal cracks at the center of the thin section (Fig. 11), and these cracks prevented the formation of a core fragment; no regions with cracks were found at either corner of the antipodal surface. The regions surrounded by major cracks are the source candidates of the largest fragment observed in Fig. 7. Usually, the core-type disruption is accompanied by thin spall fragments, as a result of spallation that occurs via a tensile wave reflected from a free surface. The thickness of the spall fragment depends on the waveform; thin fragments may be caused by a sharp wave. For a basalt target, the disruption type is classified into two types (core and cone type) according to the impact velocity. In a low-velocity region, cone-type fragmentation is present, characterized by large fragments formed not by spallation but by vertical cracks. In the case of water ice, the disruption type in the low velocity region (<1 km/s) was the cone type. In our experiments, the disruption type resembled the cone type, although the impact velocity was high enough to induce core-type disruption in the case of basalt.

As a result, it is concluded that there is no core-type disruption for water ice in a velocity range from 50 m/s to 4 km/s.

4.5. Late-Stage Equivalence

For the 50-mm ice ($M_t = 112$ g), an impact by a 7-mg projectile at 3.79 km/s resulted in $m_1/M_t = 0.05$. Notably, in Arakawa *et al.* (1995), the same m_1/M_t was made for the same size target (50 mm, $M_t = 121$ g) by a 3.2-g ice projectile at 250 m/s. Mass distribution is also very similar between these results, although made under very different impact conditions (Fig. 12). These similarities may be explained by a late-stage equivalence proposed by Diens and Walsh (1970), who showed that the shape of shock waves far from the impact point became the same when the shock waves were induced by an impact with the same value as the parameter $L_p v_i^\alpha$. In our case, α is derived as 0.85 by means of a comparison between the impact conditions. This value is larger than the 0.58 obtained by Diens and Walsh, although the difference is theoretically explained by Mizutani *et al.* (1990). According to Mizutani's theory, α is determined by the decay constant b and the parameter a related to the Hugoniot equation of state. An a of any kind of material is estimated to be 1.67 for the wide range of impact velocity considered here in, and b is estimated to be 2 for water ice in these experiments. Then α is calculated by b/a; 0.84 is obtained theoretically for α, which is consistent with the 0.85 directly derived from the impact condition. Therefore, we can conclude that $L_p v_i^{0.85}$ is the important parameter by which to present late-stage equivalence in the ice target.
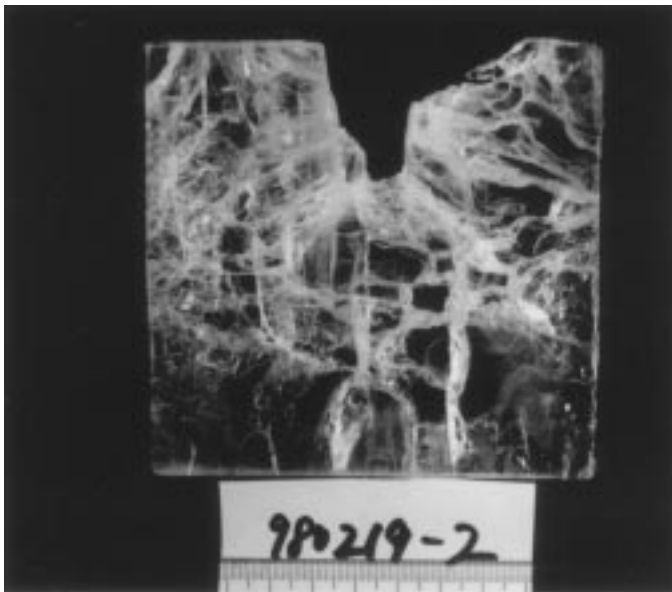
FIG. 11. Photograph of a thin section of the largest fragment for Run 219-2. The target size is 100 mm and the impact velocity is 3.97 km/s. The scale is shown by the ruler on the tag of the run number. The smallest divisions are millimeters. The section of the impact crater is observed from the top and many cracks appear below it.
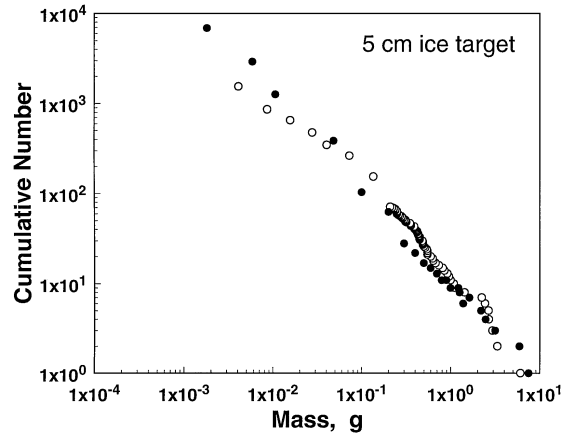
FIG. 12. Cumulative number of recovered fragments for two different experiments in our study and that of Arakawa *et al.* (1995). They used an ice target of the same size (50 mm), but the impact conditions were very different: impact velocity of 3.79 km/s and projectile mass of 7 mg, ○; impact velocity of 250 m/s and projectile mass of 3.2 g, ●. The largest fragment mass and the mass distribution of fragments were consistent between these disparate experiments.

5. IMPLICATIONS FOR REACCUMULATION CONDITIONS

Arakawa *et al.* (1995) calculated the reaccumulation condition of icy planetesimals at collision velocities slower than 500 m/s and mass ratios larger than 10^{-3}. The criterion they used for the reaccumulation is described as $V_{a-c} < \frac{1}{2} V_{esc}$, where V_{a-c} is the antipodal velocity in the center of mass system and V_{esc} is the escape velocity of the icy planetesimal. This criterion was determined in the study of Fujiwara and Tsukamoto (1980), where it was reported that 70 to 80% (by mass) of all impact fragments have ejection velocities slower than about twice the antipodal velocity for basalt. We used the same criterion to obtain the reaccumulation condition of icy planetesimals under wider impact conditions of impact velocity (from 500 m/s to 5 km/s) and mass ratio (from 10^{-2} to 10^{-5}). In addition, we illustrate the escape conditions, whereby all ejecta made by the impact cannot reaccumulate on the parent body, by using the criterion described as $V_{a-c} > V_{esc}$.

In order to derive the reaccumulation and escape conditions, we simulated collisions between icy planetesimals made of water ice with a density of 917 kg/m^3. Note here that the estimated conditions are only applicable for homogeneous solid ice bodies. If V_a is calculated by using Eqs. (3) and (4), then V_{a-c} can be described as

$$V_{a-c} = V_a - V_c = \frac{2P_0}{\rho_t C_t}\left(\frac{m_p}{M_t}\right)^n - \frac{m_p/M_t}{1 + (m_p/M_t)}V_i. \quad (9)$$

We use $n = 0.7$ for the above wide range of impact conditions as shown in Section 4.2. Figure 13 shows reaccumulation and escape conditions such as impact velocity and mass ratio, which are calculated from Eq. (9) combined with $\frac{1}{2}V_{esc} = V_{a-c}$ and $V_{esc} = V_{a-c}$ for each parent body with a radius of 2, 20, and
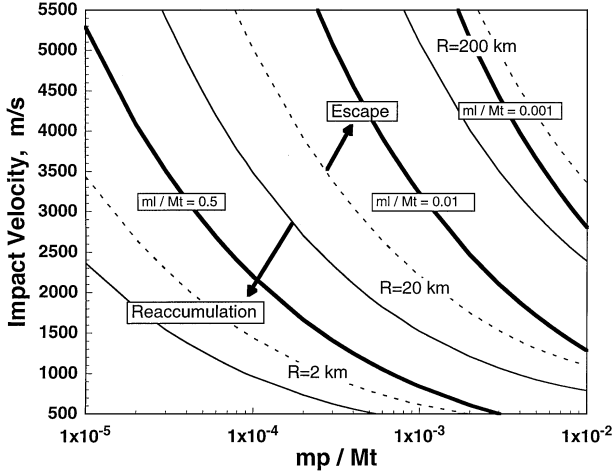
FIG. 13. Reaccumulation and escape conditions of the icy body with the density of water ice. Each curve represents the critical conditions of reaccumulation (thin solid curves) and of escape (broken curves) for parent bodies with radii of 2, 20, and 200 km, respectively. The thick solid curves represent the impact conditions corresponding to the catastrophic threshold ($m_1/M_t = 0.5$), and $m_1/M_t = 0.01$ and 0.001 (two other degrees of fragmentation).

200 km; the mass of the respective parent bodies is shown by M_t in Eq. (9). The area below the thin solid curve corresponds to the reaccumulation condition of each parent body, while the area above the broken curve corresponds to the escape condition; it is the case that all fragments escape from the parent body. In the area between the thin solid curve and the broken curve for each body, the impact fragments, except for a few tens of percents of the parent body, escape. The remaining fragments may subsequently reaccumulate to make a body somewhat smaller in size than the parent body before disruption.

The degree of fragmentation is related to m_1/M_t, and the relation of $m_1/M_t = 0.5$ is adopted for the threshold of the catastrophic disruption (Durda *et al.* 1998). P_I at this critical condition, obtained from Eq. (8), has a value of 0.26. The corresponding impact condition is shown in Fig. 13 as a thick solid curve labeled $m_1/M_t = 0.5$, and the catastrophic disruption occurs above this curve. It has been proposed in previous studies (Housen and Holsapple 1990) that impact material strength decreases with increase of the target size from laboratory scale to satellite scale. Thus, the calculated curve can be recognized as the upper limit of the impact material strength, which means that, when we consider collisions among satellite scale objects, this curve would move toward the side of lower impact velocity and lower m_p/M_t. Impact conditions corresponding to $m_1/M_t = 0.01$ and 0.001 are also shown in Fig. 13, indicated by thick solid curves.

The boundary of the reaccumulation condition for a body of $R = 20$ km is above the catastrophic threshold. Therefore, when the reaccumulation occurs at the impact condition between the catastrophic threshold and the reaccumulation boundary of $R = 20$ km, the parent body captures nearly all of the disrupted fragments and they become a rubble pile. In the case of a body of $R = 200$ km, the impact condition for which the rubble pile

is formed becomes wider than that in the case of a body of $R = 20$ km. When this large body collides with a smaller body of $R = 20$ km ($m_t/M_t = 10^{-3}$), the rubble pile is formed at impact velocities between 1 and 5 km/s. On the other hand, since both the reaccumulation and the escape boundaries of a body of $R = 2$ km is outside the area of the catastrophic disruption, the fragments never reaccumulate on the parent body and are ejected away whenever the body is disrupted catastrophically.

At an impact condition below $m_1/M_t = 1$, impact only makes a crater on the surface and large fragments are never ejected. The ejecta for which maximum velocity is almost equal to impact velocity are excavated from the crater (Table I); the size of the ejecta is usually several orders of magnitude smaller than the size of the targets. Thus, when icy bodies collide at a velocity greater than 1 km/s, the ejecta can easily escape from parent bodies smaller than 1000 km, for which escape velocity is almost 720 m/s. It is surmised that impacts at the above crater condition would contribute to the accumulation of interplanetary dust in the outer Solar System (Yamamoto and Mukai 1998).

In the outer Solar System, many small icy satellites have been discovered during exploration by the *Voyager* spacecrafts. The satellites, ranging from $R = 10$ km to 100 km, show irregular shapes, and their diameter ratio, which is defined as the ratio of the longest axis length to the shortest axis length, is found to vary beyond 2 (Hartmann 1983, p. 203). Satellites larger than 200 km are known to have a round shape because under the condition of gravity, the internal stress is higher than the ice strength. Explanations for the irregular shape of the smaller satellites remain still controversial. Fujiwara *et al.* (1978) found that the impact fragments had a large diameter ratio, the mean value of which was about 2, although the measured values fluctuated very much. We consider that the large diameter ratio of small icy satellites may be evidence that they are impact fragments.

When V_c is sufficiently smaller than V_a ($m_p/M_t < 10^{-3}$), the maximum fragment ejected from the parent body at the escape condition is estimated by using Eqs. (4) and (8), substituting V_{esc} for V_a in Eq. (4). Thus, the relation $m_1/M_t = 3.8V_{esc}^{-1.7}$ is derived. Since V_{esc} is proportional to the radius of the body, this relation is rewritten as

$$r_1 = 94R^{0.43}, \qquad (10)$$

where r_1 is the maximum fragment radius (i.e., it is assumed to have a spherical shape). Equation (10) shows that an ice fragment with $r_1 = 10$ km is made by the collision of an icy body larger than about 50 km ($m_1/M_t = 0.008$), and a fragment of $R = 100$ km is made by the collision of a body larger than about $R = 10^4$ km ($m_1/M_t = 10^{-6}$). Therefore, it is possible that an icy satellite with $R = 10$ km is a impact fragment originated by impact disruption. On the other hand, if an icy satellite with $R = 100$ km is assumed to be an impact fragment, it should have originated from the disruption of an icy body larger than 10^4 km, the size of which is 4 times as large as Ganymede or Callisto. It is problematic to assume the presence of icy satellites this large in the proto-planetary nebula, as they would have to exist

around giant planets. Therefore, we must consider other possibilities to explain the large diameter ratio of icy satellites with $R = 100$ km.

It was previously shown that the reaccumulation of bodies approximately 100 km in size was quite possible, and that the parent body became a rubble pile. When the reaccumulation occurs close to the catastrophic threshold and the parent body is disrupted into relatively large fragments ($<0.8R$), then these fragments, held captive by gravity, become the main constituent of the rubble pile. Since each fragment has a large diameter ratio, the surface of the rubble pile would have a large roughness, contributed to by the individual fragments. It is possible that this surface roughness is observed as a large diameter ratio of icy satellites.

6. SUMMARY AND CONCLUSIONS

High-velocity impacts of water ice were studied by using a two-stage light gas gun installed in a cold room ($-10°$C) in order to clarify the elementary processes of collisional disruption and to study reaccumulation and escape conditions of the impact fragments. Cubic ice targets of sizes ranging from 15 to 100 mm were impacted by a nylon projectile of 7 mg with an impact velocity from 2.3 to 4.7 km/s. We then measured the ejecta velocity and the mass distribution of the fragments. As a result, the following results were obtained.

(1) It was observed that the high-velocity fragments were ejected from the crater and their maximum velocities reached about 0.7–0.9 of the impact velocity. The angle of the ejecta curtain to the impact surface varied from $14°$ to $68°$, depending on the tilt of the projectile.

(2) We found that the antipodal velocity decreased with the target size, and this relation was described as Eq. (6). Theoretically, this relation is recognized as the shock pressure attenuation, and it is therefore concluded that shock pressure attenuates in the ice target according to the relation of $P \propto r^{-2.2}$, irrespective of a mass ratio between 10^{-3} and 10^{-5}.

(3) The cumulative number of impact fragments showed a power-law relation with their respective masses (m) at the low-mass region ($m/M_t < 10^{-3}$), and the average power index was found to be $0.64(\pm 0.06)$.

(4) m_1/M_t had a good relationship to P_I (NDIS), and this relation was analyzed in consideration with our previous findings on low-velocity impact. As a result, Eq. (8) was derived for a wide range of impact conditions (50 m/s $< v_i < 4$ km/s and $10^{-1} < m_1/M_t < 10^{-6}$).

(5) The fragmentation mode of the high-velocity impact of ice was found to be a cone type, although a core type is known to appear for basalt at the high-velocity impact. Further, the ice fragmentation mode at the low-velocity impact is also known to be a cone type (Arakawa *et al.* 1995).

The reaccumulation and the escape conditions of icy bodies in high-velocity collisions were estimated using Eq. (9) and in accordance with a previously proposed criterion. As a result, it was clarified that a rubble pile could be formed when icy bodies with a radius larger than 20 km reaccumulated. On the other hand, when icy bodies with a radius smaller than 2 km disrupted catastrophically, all fragments escaped away (i.e., did not form a rubble pile). When we apply our results to the observed small icy satellites (<10 km), it may be inferred that the small icy satellite with an irregular shape is an impact fragment that originated from a collision under the escape condition.

REFERENCES

Ahrens, T. J., and J. D. O'Keefe 1977. Equation of state and impact-induced shock-wave attenuation on the Moon. In *Impact and Explosion Cratering* (D. J. Roddy, R. O. Pepin, and R. B. Merrill, Eds.), pp. 639–656. Pergamon Press, New York.

Arakawa, M., and M. Higa 1996. Measurements of ejection velocities in collisional disruption of ice spheres. *Planet. Space Sci.* **44**, 901–908.

Arakawa, M., N. Maeno, M. Higa, Y. Iijima, and M. Kato 1995. Ejection velocity of ice impact fragments. *Icarus* **118**, 341–354.

Diens, J. K., and J. M. Walsh 1970. Theory of impact: Some general principles and the method of Eulerian codes. In *High-Velocity Impact Phenomena* (R. Kinslow, Ed.), pp. 45–104. Academic Press, New York.

Durda, D. D., R. Greenberg, and R. Jedicke 1998. Collision models and scaling laws: A new interpretation of the shape of the main-belt asteroid size distribution. *Icarus* **135**, 431–440.

Frisch, W. 1991. Hypervelocity impact experiments with water ice targets. In *Proceedings of the Workshop on Hypervelocity Impact in Space* (J. A. M. McDonnell, Ed.), pp. 7–14. University of Kent, Canterbury.

Fujiwara, A., and A. Tsukamoto 1980. Experimental study on the velocity of fragments in collisional breakup. *Icarus* **44**, 142–153.

Fujiwara, A., G. Kamimoto, and A. Tsukamoto 1977. Destruction of basaltic bodies by high-velocity impact. *Icarus* **31**, 277–288.

Fujiwara, A., G. Kamimoto, and A. Tsukamoto 1978. Expected shape distribution of asteroids obtained from laboratory impact experiments. *Nature* **272**, 602–603.

Gaffney, E. S. 1985. Hugoniot of water ice. In *Ices in the Solar System* (J. Klinger, D. Benest, A. Dollfus, and R. Smoluchowski, Eds.), pp. 119–148. Reidel, Dordrecht.

Gold, L. W. 1958. Some observations on the dependence of strain on stress in ice. *Can. J. Phys.* **36**, 1265–1275.

Hartmann, W. K. 1983. *Moons and Planets.* Wadsworth, Belmont, CA.

Housen, K. R., and K. A. Holsapple 1990. On the fragmentation of asteroids and planetary satellites. *Icarus* **84**, 226–253.

Kato, M., Y. Iijima, M. Arakawa, Y. Okimura, A. Fujimura, N. Maeno, and H. Mizutani 1992. Impact experiment on low temperature ice. In *Physics and*

Chemistry of Ice (N. Maeno and T. Hondo, Eds.), pp. 237–244. Hokkaido Univ. Press, Sapporo.

Kato, M., Y. Iijima, M. Arakawa, Y. Okimura, A. Fujimura, N. Maeno, and H. Mizutani 1995. Ice-on-ice impact experiments. *Icarus* **133**, 423–441.

Kawakami, S., H. Mizutani, Y. Takagi, M. Kato, and M. Kumazawa 1983. Impact experiments on ice. *J. Geophys. Res.* **88**, 5806–5814.

Lange, M., and T. J. Ahrens 1983. The dynamic tensile strength of ice and ice-silicate mixtures. *J. Gephys. Res.* **88**, 1197–1208.

Lange, M., and T. J. Ahrens 1987. Impact experiments in low-temperature ice. *Icarus* **69**, 506–518.

Marsh, S. P. 1980. *LASL Shock Hugoniot Data*. Univ. of California Press, Berkley.

McKinnon, W. 1989. Impact jetting of water ice, with application to the accretion of icy planetesimals and Pluto. *Geophys. Res. Lett.* **16**, 1237–1240.

Mizutani, H., Y. Takagi, and S. Kawakami 1990. New scaling law on impact fragmentation. *Icarus* **87**, 307–329.

Pierazzo, E., A. M. Vickery, and H. J. Melosh 1997. A reevaluation of impact melt production. *Icarus* **127**, 408–423.

Takagi, Y., H. Mizutani, and S. Kawakami 1984. Impact fragmentation experiments of basalt and pyrophyllites. *Icarus* **59**, 462–477.

Yamamoto, S., and T. Mukai 1998. Dust production by impacts of interstellar dust on Edgeworth–Kuiper belt objects. *Astron. Astrophys.* **329**, 785–791.